Hidden hearing loss in a hereditary peripheral neuropathy: evidence from a mouse model of Charcot Marie Tooth type 1A.

Luis R. Cassinotti; Lingchao Ji; M. Caroline Yuk; Aditi S. Desai; Nathan D. Cass; Zahara A. Amir and Gabriel Corfas*

Kresge Hearing Research Institute and Department of Otolaryngology-Head and Neck Surgery, University of Michigan, Ann Arbor, MI, United States.

* Corresponding author:
Gabriel Corfas, Ph.D.
Kresge Hearing Research Institute
The University of Michigan
Medical Sciences I Building, Rm. 5428
1150 West Medical Center Drive
Ann Arbor, MI 48109-5616
Tel: 734-615-2222
Email: corfas@med.umich.edu

Current affiliations

Lingchao Ji: Dept. of Otolaryngology, Peking University Shenzhen Hospital, China

Aditi S. Desai: University of Virginia School of Medicine, Charlottesville, Virginia, United States

Nathan D. Cass: Department of Otolaryngology, University of Kentucky, Lexington, KY, United States

Author Contributions: LRC and GC designed the research studies. LRC, LJ, MCY, ASD and NDC conducted experiments. LRC, MCY, ASD and NDC acquired data. LRC, MCY, ASD, NDC, ZAA and GC analyzed data. LRC, LJ, MCY, ASD, NDC and GC wrote the manuscript.

Competing Interest Statement: GC was a scientific founder of Decibel Therapeutics, had equity interest in the company and received compensation for consulting. The company partially supported this work.

Classification: Biological sciences (Neuroscience)

Keywords: CMT; synaptopathy; myelin; auditory nerve, heminode, node of Ranvier.

Data Availability: All data generated or analyzed during this study are included in the manuscript. Original electron microscopy and confocal images used for calculations, ABR and DPOAE recordings will be uploaded to Dryad.

Abbreviation list:

ABR: Auditory Brainstem Response

DPOAE: Distortion Product Otoacoustic Emissions

CMT: Charcot-Marie-Tooth disease

CMT1A: Charcot-Marie-Tooth type 1A

CMT1E: Charcot-Marie-Tooth type 1E

HHL: Hidden Hearing Loss

AN: Auditory Nerve

HC: Hair Cell

IHC: Inner Hair Cell

OHC: Outer Hair Cell

PMP22: Peripheral Myelin Protein 22

SGN: Spiral Ganglion Neuron

MBP: Myelin Binding Protein

NoR: Node of Ranvier

Abstract

Hidden hearing loss (HHL), a recently described auditory neuropathy characterized by normal audiometric thresholds but reduced sound evoked potentials, has been proposed to underlie hearing difficulties in noisy environments. Animal studies showing that HHL is associated with loss of inner hair cell (IHC) synapses in response to mild noise exposures and aging led to most studies of HHL focusing on IHC synaptopathy. More recently we showed that transient auditory nerve (AN) demyelination also causes HHL but without affecting IHC synapses, suggesting that demyelinating peripheral neuropathies could be a second HHL mechanism. To test this in a clinically relevant model, we studied a mouse model of Charcot-Marie-Tooth type 1A (CMT1A), the most prevalent hereditary peripheral neuropathy in humans. CMT1A mice exhibit HHL, i.e., normal auditory threshold but reduced amplitudes and longer latencies of sound-evoked compound action potential. The AN structural phenotypes of CMT1A mice are also remarkably similar to those found in mice with transient demyelination, i.e., disorganization of AN heminodes near the IHCs with minor loss of AN fibers. Our results support the hypothesis that mild disruptions of AN myelination can cause HHL, and that heminodal defects contribute to the alterations in action potential amplitudes and latencies seen in these models. Also, these findings suggest that patients with CMT1A or other peripheral neuropathies like Guillain-Barré Syndrome, are likely to suffer from HHL. Furthermore, these results suggest that studies of hearing in CMT1A patients might help in the development of robust clinical tests for HHL, which are currently lacking.

Significance Statement

Hidden Hearing Loss (HHL), an auditory disorder estimated to affect 12-15% of the adult population, is believed to impact auditory processing and hearing clarity in individuals with normal audiometric thresholds. Based on animal studies, the loss of inner hair cell synapses is currently considered its primary cause. Here we provide evidence that mild disruptions of auditory nerve myelination, i.e., disorganization of auditory nerve heminodes, can also cause HHL. Our results suggest that patients suffering from Charcot-Marie-Tooth type 1A, the most common hereditary peripheral neuropathy, are likely to experience HHL. Studies of hearing in CMT1A patients might thus help in the development of robust clinical tests for HHL, which are currently lacking.

Introduction

Many people report having hearing difficulty in noisy environments despite presenting with normal audiometric thresholds (1-5). There is substantial evidence associating this auditory pathology with aging or with a history of “mild” noise exposures that only induce temporary increases in hearing thresholds (6-13). Studies on animal models demonstrated that such mild noise-exposures do not result in hair cell (HC) loss but instead destroy a subset of synapses between inner hair cells (IHCs) and spiral ganglion neurons (SGNs) (14). Moreover, in animals, IHC synaptopathy precedes HC loss during aging, even in the absence of noise over-exposure (14-20). Physiological recordings show that animals with IHC synaptopathy have normal hearing thresholds but reduced amplitudes of sound-evoked potentials (15, 16, 18, 21), a condition that has been termed 'hidden hearing loss' (HHL) (22, 23). Importantly, histopathological studies have shown that age-related synaptopathy also occurs in humans (24, 25), suggesting that HHL might contribute to the hearing difficulties in people with normal thresholds. The compelling information generated from noise-exposed and aging animals led to the sense that IHC synaptopathy might be the only cause of HHL. However, more recently, we showed that transient auditory nerve (AN) demyelination causes a similar hearing deficit in mice without affecting IHC synapses (26), suggesting that demyelinating peripheral neuropathies could also cause HHL. To begin to test this possibility in clinically relevant experimental models, we focused on mouse models of Charcot Marie Tooth type 1 (CMT1) disease, the most common hereditary peripheral neuropathy in humans.

CMT1 is a type of CMT, a group of hereditary peripheral neuropathies that are associated with a range of genetic lesions and pathogenic mechanisms (27, 28). CMT1, which is considered as a demyelinating CMT, includes multiple subtypes (from A to E) arising from alterations in diverse myelin-related genes (29). CMT1A, the predominant subtype (>50% of CMT1 cases), is caused by the duplication of *PMP22*, a gene that encodes an integral membrane glycoprotein essential for the formation and maintenance of compact myelin (30, 31). Interestingly, recent studies suggest that CMT1A patients might suffer from hearing difficulties consistent with HHL (32-35). However, this has not been confirmed due to the lack of validated clinical HHL tests in humans (23, 36). In contrast, patients with CMT1E, which is caused by a wide variety of *PMP22* point mutations (29) and lead to more severe neuropathy phenotypes with earlier onset, suffer from overt hearing loss (elevated auditory thresholds) (37-41). Furthermore, a CMT1E mouse model, Trembler-J, has been shown to have profound deafness including AN fiber loss (42, 43).

Here we used CMT1A (44) and CMT1E (a.k.a. Trembler-J) (45) mouse models to explore the specific impact of these hereditary peripheral neuropathies on inner ear structure and function. As expected from findings in other peripheral nerves (44, 46-51), both models exhibit distinct AN structural phenotypes, which are less severe in CMT1A mice. Our functional studies demonstrate that, as shown by others (42, 43), CMT1E mice present with early-onset overt hearing loss with profound auditory threshold shifts. In contrast, CMT1A mice exhibit the distinct electrophysiological features of HHL, i.e., normal auditory thresholds but reduced sound-evoked compound action potential amplitudes. As we previously found in mice with transient demyelination (26), sound-evoked compound action potential latencies are longer in CMT1A mice, a defect not present in mice with IHC synaptopathy (14, 26). At the structural level, the cochlear defects of CMT1A mice are remarkably similar to those we found in mice after transient AN demyelination (26), involving disorganization of AN heminodes near the IHCs.

Together, these results support the hypothesis that mild disruptions of AN myelination can cause HHL, and that AN heminodal defects are responsible for the reduced amplitude and longer latencies of sound-evoked compound action potentials seen in the mouse models (26, 52). Our results also support the notion that CMT1A patients are likely to suffer from HHL, and that this type of hearing disorder might affect patients with other types of peripheral

neuropathies, including Guillain-Barré Syndrome. Furthermore, our confirmation of electrophysiological and structural elements of HHL in the CMT1A mouse suggest that studies of hearing in CMT1A patients might help in the design and validation of robust clinical tests for HHL and thereby circumvent some of the difficulties encountered with self-reporting on historical noise exposure and noise-induced HHL in humans, which have resulted in conflicting conclusions (1, 36, 53).

Results

CMT1A mice have progressive hidden hearing loss.

To determine the auditory phenotypes of CMT1A and CMT1E mice, we recorded distortion product otoacoustic emissions (DPOAEs) and auditory brainstem responses (ABRs) at 1, 2, 3 and 4 months of age (Fig. 1A) in the mutants and their wildtype C57BL/6J littermate controls. ABRs reflect the sound-evoked electrical activity along the ascending auditory pathway, from the activation of IHCs and SGNs in the cochlea up to the inferior colliculus in the central nervous system. ABR thresholds provide information about hearing sensitivity whereas the amplitude of the first peak of the ABR waveform reflects the magnitude of the sound evoked SGN activation. DPOAEs are sounds generated by the inner ear in response to sound stimulation, reflecting the activity of outer hair cells (OHCs). Together, these measurements provide insights into the integrity of the cochlea. For example, increased ABR thresholds without a change in DPOAEs provides strong evidence for auditory neuropathy, i.e., defects in the function of IHCs and/or SGNs without OHC defects.

As anticipated for C57BL/6J wildtypes, control mice show stable DPOAE and ABR thresholds during their first 4 months of life (Fig. 1B-C), and a small but statistically significant age-related decline in ABR peak I amplitudes (Fig. 1D; Fig. 2, Fig. S1 and Fig. S2A). Their ABR peak I latencies become shorter by 2 months of age, possibly due to the maturation of AN myelination (54, 55) (Fig. 1E and Fig. S2B). Consistent with published reports (42, 43), CMT1E mice have higher ABR thresholds at all ages and frequencies tested (Fig. 1C) while their DPOAE thresholds are mildly increased only at 4 months of age (Fig. 1B), compared to wildtype mice. Furthermore, CMT1E ABR peak I amplitudes are considerably lower and the latencies longer than in wildtype mice (Fig. 1D-E; Fig. 2 and Fig. S1). These findings support a profound auditory neuropathy as early as 1 month of age in CMT1E mice, which then progresses to include OHC dysfunction. In contrast, CMT1A mice have normal ABR and DPOAE thresholds at all ages (Fig. 1B-C), but their ABR peak I amplitudes are already smaller than those in wildtypes by 1 month of age and decline further over time (Fig. 1D; Fig. 2 and Fig. S1), the hallmarks of progressive HHL. Moreover, ABR peak I latencies are longer than those in wildtype mice at 2 month of age and do not get shorter at later time points (Fig. 1E and Fig. 2), suggesting a lack of myelin maturation. The ABR waveforms (Fig. 2) also show that the summating potentials (SP), which represent the activation of IHCs, are normal in CMT1A mice but are significantly reduced in 4-month-old CMT1E, likely reflecting the OHC dysfunction seen at this age. The waveforms also illustrate that CMT1E mice have a progressive decrease in signaling along the ascending auditory pathway, whereas CMT1A mice have a milder phenotype that includes relatively small delays and reduced amplitudes of peaks II, III, and IV at 1 and 2 months of age, but that by 4 months of age show increased amplitudes of peaks III and IV, suggestive of the homeostatic compensation in the auditory brainstem and midbrain see in animals with partial peripheral deafferentation (56-60). Remarkably, after 2 months of age, the functional defects in CMT1A are identical to those we found in mice following transient demyelination, i.e., normal threshold, reduced ABR peak I amplitudes, and longer peak I latencies (26).

CMT1A and CMT1E mice have distinct inner ear axonal and myelin pathologies.

To explore the structural basis for the functional phenotypes in the CMT1 mice, inner ears were harvested after the final ABR/DPOAE recording and subjected to several levels of histological analysis. Transmission electron microscopy of cross sections through the osseous spiral lamina (the bony structure encasing the AN fibers) in the mid-cochlear region (~16 kHz) demonstrated that CMT1A cochleas have a small but significant reduction in myelinated axon density (18 %) whereas axonal loss is much larger in CMT1E mice (~78 %) (Fig. 3A-B). Interestingly, while the diameters of the remaining axons in CMT1E cochleas are like those seen in wildtypes, axonal diameters in CMT1A ears are reduced (Fig. 3C). In contrast, measurements of g-ratio, i.e., the ratio of the inner versus outer layer diameter of the myelin sheath, reflect thinner myelin (larger g-ratio) in CMT1E auditory axons (Fig. 3D, E). The phenotype is more complex and heterogenous in CMT1A cochleas, in which small diameter axons exhibit thicker myelin, resulting in a steepening of the regression line in the g-ratio vs axon diameter graph (Fig. 3D, E). These results demonstrate that CMT1A and CMT1E mutations cause distinct AN axonal and myelin structural changes which are similar to those seen in other peripheral nerves (44, 46-51), with CMT1A mice presenting a less severe phenotype.

CMT1A results in AN heminodes abnormalities.

The auditory physiology phenotypes in CMT1A mice (Figs. 1, 2 and S1), i.e., normal threshold, reduced ABR peak I amplitudes, and longer peak I latencies, are remarkably similar to those we previously recorded in mice that had undergone remyelination after transient ablation of Schwann cells (26). In the latter case, the enduring AN structural abnormality that correlates with the physiological findings is disarray of AN heminodes, the nodal structures at the peripheral ends of the terminal Schwann cells adjacent to the IHCs. AN heminodes have been proposed to function as the SGN action potential initiation site, and to play a critical role in synchronous neural transmission (52, 61-63). To evaluate the impact of CMT1A and CMT1E on nodal structures, we used laser confocal microscopy with antibodies targeted to Ankyrin-G (a nodal protein marker (64)), Caspr (a paranodal marker (64)), and Myelin Basic Protein (MBP) to visualize myelin (65) on cochleas from 4-month-old mice.

Whereas AN heminodes in wildtype mice are tightly clustered within the 20 µm segments of the myelinated axon closest to the IHCs, heminode clustering is disrupted in CMT1A cochleas (Fig. 4A, B), with elongated Caspr-positive regions and Ankyrin-G-positive regions located further from the peripheral end of the heminodes relative to those in wildtypes. Furthermore, similar to what we observed following transient demyelination-remyelination (26), there are numerous nodes of Ranvier (NoR) in the area directly adjacent to heminodes in CMT1A cochleas, whereas very few NoR are present in this area in wildtypes (Fig. 4B and 4D). Nevertheless, the overall NoR density in the peripheral AN processes of CMT1A mice is similar to that in wildtypes (Fig. 4C and 4E), suggesting that Schwann cell internode lengths are not affected in these mutants. As can be expected from the severe AN axonal loss in CMT1E mice, the heminodal disruption in these mutants is more severe (Fig. 4A and B). Accurate quantification of heminodes and NoR density in CMT1E mice was not possible due to the profound AN axon loss.

CMT1A and CMT1E mice have different degrees of IHC-SGN synapse loss without affecting hair cell number.

Finally, to evaluate the potential contribution of HC or IHC synapse loss to the auditory physiology defects of the mutant mice, we quantified the number of IHCs and OHCs as well as IHC-SGN synaptic density in 4-month-old mice from each cohort. Notably, IHC and OHC survival were not affected by either of the two CMT1 mutations (Fig. 5A and 5C). In concordance with the severe axonal loss (Fig. 3A and 3B), CMT1E mutants have a large (58–61 %) reduction in IHC-SGN synaptic density compared with wildtypes (Fig. 5B and 5D). In

contrast, CMT1A mice exhibit a more modest (15 %) reduction in IHC-SGN synaptic density in the mid-high frequency area (Fig. 5B and 5D), which may also reflect the small degree of axonal loss in these mutants (Fig. 3A and 3B).

Discussion

The concept of HHL was first proposed in 2011 (66), and since then research on the mechanism of its pathogenesis has centered around IHC synaptopathy (14). Here we provide evidence that a mouse model of CMT1A, the most prevalent hereditary peripheral myelin disorder, exhibits the functional hallmarks of HHL, i.e., normal auditory thresholds but reduced ABR peak I amplitudes. The observation that a mouse model of CMT1E, which is caused by different alterations in the same gene as CMT1A (*Pmp22*), has overt hearing loss (like some CMT1E patients) together with a distinct set of structural deficits in the cochlea, corroborates the specificity of the CMT1A phenotype. Furthermore, the notion that myelin disorders are an alternative etiology for HHL is supported by the remarkable phenotypic similarities between mice following transient AN demyelination (26) and the CMT1A model, i.e., normal ABR and DPOAE thresholds, reduced ABR peak I amplitudes together with longer peak I latencies. This idea is also ratified by the fact that a unique feature like the longer ABR peak I latencies observed in both models are absent in mice with noise-induced or age-related IHC synaptopathy (14, 26).

Here we also show that, like in mice following transient AN demyelination (26), cochlear heminodes are disrupted and NoR are mislocalized in CMT1A mice. Moreover, this structural phenotype correlates with the reduced sound evoked SGN activation in both models, supporting the crucial role of the AN heminodes as the SGN action potential initiation site, and its importance for fast and synchronized AN spike generation as has been previously suggested in computational models or electrophysiological and immunostaining studies (52, 61-63).

The distinct AN myelin and axonal phenotypes in each CMT1 mouse model are also remarkably similar to those observed in other peripheral nerves, suggesting that the specific *Pmp22* mutations exert common pathological effects across myelinating glia. For example, AN in CMT1A cochleas exhibit an increased proportion of smaller axons, a slight reduction in the number of myelinated fibers, hypermyelination of small diameter fibers, and a steepening of the regression line in the g-ratio vs axon diameter graph, all features that have been reported in other peripheral nerves of this mouse model and also in CMT1A rat models (44, 46-48). In contrast, sciatic nerves from CMT1E mice exhibit hypomyelination, much like what we and others have observed in the cochlea of this model (49-51). Furthermore, the AN phenotypes in both models are consistent with findings in other nerves in CMT1 patients (67).

Given the lack of validated diagnostic tools for HHL in humans (23), our findings in the CMT1A mouse model provide strong support for the handful of clinical observations suggesting CMT1A patients have HHL-like phenotypes. An early study of children with CMT1A reported that most have normal audiological thresholds, but some have lower ABR amplitudes and longer latencies (34). Furthermore, more than 60% of these children have defects in auditory perception, temporal processing, and speech recognition, consequences that have now been predicted for humans with HHL (1-9). More recent studies reported that adult CMT1A patients have normal auditory thresholds, but defects in speech perception in noisy backgrounds, reflected by lower temporal and spectral resolution than healthy controls (32, 33). Importantly, our results also suggest that studying patients with genetic disorders such as CMT1A is likely to facilitate the development of better tests for HHL that could be validated using the power of phenotype-genotype relationships.

The auditory function deficits of CMT1A and CMT1E mice are profoundly different, but in each case are similar to those seen in patients with the respective mutations (32-35, 37-41, 68).

Thus, we infer that it is likely that the cochlear structural phenotypes in each patient population correlate to those we see in each mouse model as well. Specifically, our findings suggest that CMT1E patients most likely have severe SGN neuron loss, whereas CMT1A patients are likely to retain most SGNs but have heminode disruptions. If this is the case, it would imply that CMT1E patients are unlikely to benefit much from hearing aids or cochlear implants, whereas CMT1A patients might be helped by hearing augmentation. This could in part explain the different efficacy outcomes observed in some CMT cochlear implanted patients (69, 70). In the same direction, and given the growing evidence showing that hearing loss can contribute to cognitive decline and dementia (71-73), it could be also important that neurologists who care for peripheral neuropathy patients include auditory testing in clinical workups and consider hearing enhancement devices in treatment. Furthermore, our observations that a mouse model of myelinopathy has the hallmarks of HHL suggest that this might be a frequent comorbidity in other peripheral demyelinating neuropathies, e.g., Guillain-Barre Syndrome. In this context, therapies that promote AN remyelination and heminode reorganization could help to prevent or slow the progression of hearing impairments associated with CMT1A or other peripheral demyelinating neuropathies (74-78).

Materials and Methods

Animals

B6.Cg-Tg (PMP22) C3Fbas/J mice (a.k.a. PMP22-C3 or C3-PMP, here termed CMT1A; The Jackson Laboratory, stock #030052), B6.D2-pmp22Tr-j/J mice (a.k.a. Trembler-J, here termed CMT1E, The Jackson Laboratory, stock #002504) and C57BL/6J wild type littermates (1 to 4 months old, male and female) were used in this study. CMT1A mice express 3 copies of wildtype human peripheral myelin protein 22 (PMP22) gene, mimicking CMT1A (44). CMT1E mice have a semi-dominant point spontaneous mutation, i.e., a T to C transition at nucleotide position 47, resulting in the substitution of a leucine by a proline in the first transmembrane domain of the PMP22 protein (45). This point mutation causes peripheral demyelination that mimics CMT1E disease. All animal procedures were approved by the Institutional Animal Care and Use Committee of the University of Michigan, and all experiments were performed in accordance with relevant guidelines and regulations.

Auditory function tests

ABRs and DPOAEs were performed on mice anesthetized with a mixture of ketamine (100 mg/kg, i.p.) and xylazine (20 mg/kg, i.p.). All groups of animals were tested at 1, 2, 3 and 4 months of age.

For ABR recordings, acoustic stimuli were delivered through a closed acoustic system, consisting of two sound sources (CDMG15008-03A, CUI) and an electret condenser microphone (FG-23329-PO7, Knowles) as an in-dwelling probe microphone. Three needle-electrodes were placed into the skin at the dorsal-midline: one close to the neural crest, one behind the left pinna and one at the base of the tail (ground). ABR potentials were evoked with 5 ms tone pips (0.5 ms rise–fall, with a $\cos^2$ envelope, at 40 s^{-1}) delivered to the eardrum at log-spaced frequencies from 5.6 kHz to 42.25 kHz. The response was amplified (10,000X) and filtered (0.3–3 kHz) with an analog-to-digital board in a PC-based data-acquisition system. The sound level was raised in 5 dB steps from 20 to 80 dB SPL. At each level, 1024 responses were averaged (with stimulus polarity alternated) after “artefact rejection” above 15 μV.

DPOAEs, in response to two primary tones of frequency f1 and f2, were recorded at (2 x f1) - f2, with f2/f1 = 1.2, and the f2 level 10 dB lower than the f1 level. Stimuli were raised in 5 dB steps from 20 to 80 dB. The ear-canal sound pressure was amplified and digitally sampled at 4 μs intervals. DPOAE thresholds were defined as the lower SPL where (2f1-f2) - (2f1-f2Nse) > 0.

Both ABR and DPOAE recordings were performed using EPL cochlear function test suite (Mass Eye and Ear, Boston, MA, USA). ABR thresholds, ABR peak I amplitudes and latencies, ABR waveforms and DPOAE thresholds were analyzed with ABR peak Analysis software (Mass Eye and Ear, Boston, MA, USA) and Microsoft Excel.

Plastic sections and transmission electron microscopy

Inner ear tissues from 4-month-old CMT1A, CMT1E and wildtype mice were dissected and fixed in 1.25 % paraformaldehyde 2.5 % glutaraldehyde 100 mM cacodylate overnight, followed by osmification in 1 % osmium tetroxide for 45 min and decalcification in 5 % EDTA 1 % glutaraldehyde 0.1M PBS for 5 days. Cochleae were microdissected and whole mount tissues were gradually dehydrated in ethanol (70 %, 95 % and 100 % steps) and embedded in araldite resin. The embedded samples were degassed for 2 h and hardened at 60°C for 5 days before ultra-thin (70 nm) sectioning for transmission electron microscopy. Ultra-thin sections containing 16 kHz cochlear region were sequentially post-stained with 6 % w/v uranyl acetate and 4.4 % w/v lead citrate. Transmission electron microscopy was performed on JEOL 1400-plus electron microscope (JEOL USA, Peabody, MA). Multiple non-overlapping regions of the AN fibers cross-sections were imaged at 600X, 3000X and 10000X magnification.

The circumference of each axon and axon + myelin sheath were measured using ImageJ software g-ratio plugin (version 1.53c, NIH, MD) on 3000X magnification images. g-ratios were calculated as g-ratio = (axon area)/(axon area + myelin sheath area). Axon diameters were calculated using the same software. Axons with circularity ($4 \times \pi \times \text{area}/\text{perimeter}^2$) under 0.6 were excluded from analysis. Myelinated axon densities were calculated by manual count on 600X magnification images and normalized to 100 μm^2. All electron microscopy images are representative of 3 individual mice per group.

Immunostaining and confocal imaging

Inner ear tissues from 4-month-old CMT1A, CMT1E and wildtype mice were dissected and fixed in 4 % paraformaldehyde in 0.01M phosphate-buffered saline (PBS) for 2 h at room temperature, followed by decalcification in 5 % EDTA at 4 °C for 5 days. Then, cochlear tissues were microdissected and permeabilized by freeze–thawing in 30% sucrose in PBS. The microdissected tissues were incubated in blocking buffer containing 5 % normal horse serum and 0.3 % Triton X-100 in PBS for 1 h. Tissues were then incubated in primary antibodies (diluted in 1 % normal horse serum and 0.3 % Triton X-100 in PBS) at 37 °C overnight. The primary antibodies used in this study were as follows; for nodes of Ranvier, heminodes and myelin staining: anti-Caspr clone K65/35 (NeuroMab, Davis, CA; 1:1000), anti-Ankyrin G (gift of Paul Jenkins laboratory; 1:500), anti-MBP (Millipore, Billerica, MA; 1:1000; catalog no. MAB386); for hair cells and IHC-SGN synapses: anti-Ctbp2 (BD Biosciences, San Jose, CA; 1:200; catalog no. 612044), anti-GluR2 (Millipore, Billerica, MA; 1:1000; catalog no. MAB397) and anti-MyoVIIa (Proteus Biosciences, Ramona, CA; 1:100; catalog no. 25-6790). Tissues were then incubated with appropriate Alexa Fluor-conjugated fluorescent secondary antibodies (Invitrogen, Carlsbad, CA; 1:1000 diluted in 1% normal horse serum and 0.3% Triton X-100 in PBS; for nodes of Ranvier, heminodes and myelin: AF488 IgG1 catalog no. A-21121; AF568 catalog no. A11036; AF647 catalog no. A-21247; for hair cells and IHC-SGN synapses: AF488 IgG2a catalog no. A-21131; AF568 IgG1 catalog no. A-21124; AF647 IgG catalog no. A-21244) for 1 h at room temperature. The tissues were mounted on microscope slides in ProLong Diamond Antifade Mountant (Thermo Fisher Scientific). All pieces of each cochlea were imaged at low power (10X magnification) to convert cochlear locations into frequency (tonotopic mapping) using a custom plug-in to ImageJ (1.53c NIH, MD) available at the website of the Eaton-Peabody Laboratories (EPL). Cochlear tissues from 8, 16 and 32 kHz regions were used

for further analyses. Confocal z-stacks of cochlear tissues were taken using a Leica SP8 confocal microscope.

Nodes of Ranvier and heminodal structure z-stacks (0.3 μm step size) were taken under 63X (+ 4.61X optical zoom) or 40X magnification (for low magnification images) at the 16 kHz cochlear region. ImageJ/Fiji software (version 1.53c, NIH, MD) was used for z-stack processing and quantification of nodes of Ranvier presence either in the 20 μm below the heminodal zone or in the osseous spiral lamina region. One cochlea from each individual animal was imaged for each experiment, with 3 adjacent images acquired at each specific cochlear region. For nodes of Ranvier quantification, the number of nodes of Ranvier in each sample was counted manually using ImageJ/Fiji software multi-point counter tool. For figures, one representative image was selected from amongst the 12–48 images.

Images for hair cell counts were taken under 40X magnification. For inner hair cell synapse counts, z-stacks (0.3 μm step size) were taken under 63X (+2.4X optical zoom) magnification spanning the entire IHC height to ensure all synapses were imaged. Imaging and analyses of cochlear hair cells and synapses were performed as previously described in (79). Briefly, ImageJ/Fiji software (version 1.53c, NIH, MD) was used for image processing and quantification. One cochlea from each of three to eight animals was imaged for each experiment, with 3 adjacent images acquired at each specific cochlear region. For hair cell quantification, the number of inner and outer hair cells at specific cochlear regions in each animal was determined based on the MyoVIIa channel and counted manually using ImageJ/Fiji software multi-point counter tool. For synapse counts, CtBP2 and GluR2 puncta in each image stacks were also captured and counted manually using ImageJ/Fiji software multi-point counter tool. Synaptic counts of each z-stack were divided by the number of IHCs, which could be visualized by staining of MyoVIIa antibody. Each individual image usually contained 8–10 IHCs. For figures, one representative image was selected from amongst the 9–24 images from the specific frequency shown.

Statistical Analysis

Graphics and statistical tests were performed using GraphPad Prism version 9.3.1 for Windows (GraphPad Software, www.graphpad.com). Data sets with normal distributions were analyzed with parametric tests whereas non-parametric tests were used for sets that did not conform to normality criteria. We used two-way ANOVA, followed by Tukey's multiple comparisons test to compare either DPOAE thresholds, ABR thresholds, ABR peak I amplitudes or latencies at each time point (1, 2, 3 and 4 months) among CMT1A, CMT1E and wildtype mice (Fig. 1B-E and Fig. S2). Quantification of myelinated axon densities was analyzed by Kruskal-Wallis test followed by Dunn's multiple comparisons test (Fig. 3B). Quantification of axon diameters and g-ratios were analyzed by one-way ANOVA followed by Tukey's multiple comparisons test (Fig. 3C-D). Simple linear regression of axon diameters vs g-ratios and statistical differences among slopes were obtained with GraphPad Prism (Fig. 3E). Quantification of nodes of Ranvier density in either the 20μm below the heminodal area or in the osseous spiral lamina region were analyzed by two-tailed t-test (Fig. 4D-E). Quantification of inner and outer hair cells was analyzed by Kruskal-Wallis test followed by Dunn's multiple comparisons test (Fig. 5C). Quantification of IHC-SGNs synapse density was analyzed by one-way ANOVA followed by Sidak's multiple comparisons test (Fig. 5D). All $p < 0.05$ were considered as statistically significant.

Acknowledgments

This work was supported by NIH R01DC018500 (GC) and a grant from Decibel Therapeutics.

References

1. H. M. Bharadwaj, S. Verhulst, L. Shaheen, M. C. Liberman, B. G. Shinn-Cunningham, Cochlear neuropathy and the coding of supra-threshold sound. *Front Syst Neurosci* **8**, 26 (2014).
2. S. Gordon-Salant, Hearing loss and aging: new research findings and clinical implications. *J Rehabil Res Dev* **42**, 9-24 (2005).
3. J. H. Grose, S. K. Mamo, Processing of temporal fine structure as a function of age. *Ear Hear* **31**, 755-760 (2010).
4. C. Halpin, A. Thornton, M. Hasso, Low-frequency sensorineural loss: clinical evaluation and implications for hearing aid fitting. *Ear Hear* **15**, 71-81 (1994).
5. D. Ruggles, H. Bharadwaj, B. G. Shinn-Cunningham, Normal hearing is not enough to guarantee robust encoding of suprathreshold features important in everyday communication. *Proc Natl Acad Sci U S A* **108**, 15516-15521 (2011).
6. L. S. Alvord, Cochlear dysfunction in "normal-hearing" patients with history of noise exposure. *Ear Hear* **4**, 247-250 (1983).
7. T. Kujala *et al.*, Long-term exposure to noise impairs cortical sound processing and attention control. *Psychophysiology* **41**, 875-881 (2004).
8. U. A. Kumar, S. Ameenudin, A. V. Sangamanatha, Temporal and speech processing skills in normal hearing individuals exposed to occupational noise. *Noise Health* **14**, 100-105 (2012).
9. M. C. Liberman, M. J. Epstein, S. S. Cleveland, H. Wang, S. F. Maison, Toward a Differential Diagnosis of Hidden Hearing Loss in Humans. *PLoS One* **11**, e0162726 (2016).
10. M. A. Stone, B. C. Moore, H. Greenish, Discrimination of envelope statistics reveals evidence of sub-clinical hearing damage in a noise-exposed population with 'normal' hearing thresholds. *Int J Audiol* **47**, 737-750 (2008).
11. M. K. Pichora-Fuller, P. E. Souza, Effects of aging on auditory processing of speech. *Int J Audiol* **42 Suppl 2**, 2S11-16 (2003).
12. D. R. Frisina, R. D. Frisina, Speech recognition in noise and presbycusis: relations to possible neural mechanisms. *Hear Res* **106**, 95-104 (1997).
13. J. R. Dubno, D. D. Dirks, D. E. Morgan, Effects of age and mild hearing loss on speech recognition in noise. *J Acoust Soc Am* **76**, 87-96 (1984).
14. S. G. Kujawa, M. C. Liberman, Adding insult to injury: cochlear nerve degeneration after "temporary" noise-induced hearing loss. *J Neurosci* **29**, 14077-14085 (2009).
15. S. G. Kujawa, M. C. Liberman, Synaptopathy in the noise-exposed and aging cochlea: Primary neural degeneration in acquired sensorineural hearing loss. *Hear Res* **330**, 191-199 (2015).
16. H. W. Lin, A. C. Furman, S. G. Kujawa, M. C. Liberman, Primary neural degeneration in the Guinea pig cochlea after reversible noise-induced threshold shift. *J Assoc Res Otolaryngol* **12**, 605-616 (2011).
17. L. Liu *et al.*, Silent damage of noise on cochlear afferent innervation in guinea pigs and the impact on temporal processing. *PLoS One* **7**, e49550 (2012).
18. E. Lobarinas, C. Spankovich, C. G. Le Prell, Evidence of "hidden hearing loss" following noise exposures that produce robust TTS and ABR wave-I amplitude reductions. *Hear Res* **349**, 155-163 (2017).
19. L. Shi *et al.*, Noise induced reversible changes of cochlear ribbon synapses contribute to temporary hearing loss in mice. *Acta Otolaryngol* **135**, 1093-1102 (2015).
20. Q. Song *et al.*, Coding deficits in hidden hearing loss induced by noise: the nature and impacts. *Sci Rep* **6**, 25200 (2016).

21. D. Mohrle *et al.*, Loss of auditory sensitivity from inner hair cell synaptopathy can be centrally compensated in the young but not old brain. *Neurobiol Aging* **44**, 173-184 (2016).
22. M. C. Liberman, Hidden Hearing Loss. *Sci Am* **313**, 48-53 (2015).
23. D. C. Kohrman, G. Wan, L. Cassinotti, G. Corfas, Hidden Hearing Loss: A Disorder with Multiple Etiologies and Mechanisms. *Cold Spring Harbor Perspectives in Medicine* **10**, a035493 (2020).
24. L. M. Viana *et al.*, Cochlear neuropathy in human presbycusis: Confocal analysis of hidden hearing loss in post-mortem tissue. *Hear Res* **327**, 78-88 (2015).
25. P. Z. Wu *et al.*, Primary Neural Degeneration in the Human Cochlea: Evidence for Hidden Hearing Loss in the Aging Ear. *Neuroscience* **407**, 8-20 (2019).
26. G. Wan, G. Corfas, Transient auditory nerve demyelination as a new mechanism for hidden hearing loss. *Nature Communications* **8**, 14487 (2017).
27. P. J. Dyck, E. H. Lambert, Lower motor and primary sensory neuron diseases with peroneal muscular atrophy. II. Neurologic, genetic, and electrophysiologic findings in various neuronal degenerations. *Arch Neurol* **18**, 619-625 (1968).
28. A. M. Rossor, J. M. Polke, H. Houlden, M. M. Reilly, Clinical implications of genetic advances in Charcot-Marie-Tooth disease. *Nat Rev Neurol* **9**, 562-571 (2013).
29. S. Ramchandren, Charcot-Marie-Tooth Disease and Other Genetic Polyneuropathies. *Continuum (Minneap Minn)* **23**, 1360-1377 (2017).
30. J. Li, B. Parker, C. Martyn, C. Natarajan, J. Guo, The PMP22 gene and its related diseases. *Mol Neurobiol* **47**, 673-698 (2013).
31. G. J. Snipes, U. Suter, A. A. Welcher, E. M. Shooter, Characterization of a novel peripheral nervous system myelin protein (PMP-22/SR13). *J Cell Biol* **117**, 225-238 (1992).
32. J. E. Choi *et al.*, Hidden hearing loss in patients with Charcot-Marie-Tooth disease type 1A. *Sci Rep* **8**, 10335 (2018).
33. J. E. Choi *et al.*, Psychoacoustics and neurophysiological auditory processing in patients with Charcot-Marie-Tooth disease types 1A and 2A. *Eur J Neurol* **27**, 2079-2088 (2020).
34. G. Rance *et al.*, Auditory function in children with Charcot-Marie-Tooth disease. *Brain* **135**, 1412-1422 (2012).
35. W. I. Verhagen *et al.*, Sensorineural hearing impairment in patients with Pmp22 duplication, deletion, and frameshift mutations. *Otol Neurotol* **26**, 405-414 (2005).
36. C. J. Plack *et al.*, Toward a Diagnostic Test for Hidden Hearing Loss. *Trends Hear* **20** (2016).
37. I. S. Joo, C. S. Ki, S. Y. Joo, K. Huh, J. W. Kim, A novel point mutation in PMP22 gene associated with a familial case of Charcot-Marie-Tooth disease type 1A with sensorineural deafness. *Neuromuscul Disord* **14**, 325-328 (2004).
38. M. J. Kovach *et al.*, Anticipation in a unique family with Charcot-Marie-Tooth syndrome and deafness: delineation of the clinical features and review of the literature. *Am J Med Genet* **108**, 295-303 (2002).
39. M. J. Kovach *et al.*, A unique point mutation in the PMP22 gene is associated with Charcot-Marie-Tooth disease and deafness. *Am J Hum Genet* **64**, 1580-1593 (1999).
40. M. Luigetti, M. Zollino, G. Conti, A. Romano, M. Sabatelli, Inherited neuropathies and deafness caused by a PMP22 point mutation: a case report and a review of the literature. *Neurol Sci* **34**, 1705-1707 (2013).
41. D. Kabzinska, E. Sinkiewicz-Darol, I. Hausmanowa-Petrusewicz, A. Kochanski, Charcot-Marie-Tooth type 1A disease caused by a novel Ser112Arg mutation in the PMP22 gene, coexisting with a slowly progressive hearing impairment. *J Appl Genet* **51**, 203-209 (2010).

42. R. Zhou, P. J. Abbas, J. G. Assouline, Electrically evoked auditory brainstem response in peripherally myelin-deficient mice. *Hear Res* **88**, 98-106 (1995).
43. R. Zhou, J. G. Assouline, P. J. Abbas, A. Messing, B. J. Gantz, Anatomical and physiological measures of auditory system in mice with peripheral myelin deficiency. *Hear Res* **88**, 87-97 (1995).
44. C. Verhamme *et al.*, Myelin and axon pathology in a long-term study of PMP22-overexpressing mice. *J Neuropathol Exp Neurol* **70**, 386-398 (2011).
45. U. Suter *et al.*, A leucine-to-proline mutation in the putative first transmembrane domain of the 22-kDa peripheral myelin protein in the trembler-J mouse. *Proc Natl Acad Sci U S A* **89**, 4382-4386 (1992).
46. Y. Bai *et al.*, Treatment with IFB-088 Improves Neuropathy in CMT1A and CMT1B Mice. *Mol Neurobiol* **59**, 4159-4178 (2022).
47. R. Fledrich *et al.*, Soluble neuregulin-1 modulates disease pathogenesis in rodent models of Charcot-Marie-Tooth disease 1A. *Nat Med* **20**, 1055-1061 (2014).
48. R. Prior *et al.*, HDAC3 Inhibition Stimulates Myelination in a CMT1A Mouse Model. *Mol Neurobiol* **59**, 3414-3430 (2022).
49. A. M. Robertson, R. H. King, J. R. Muddle, P. K. Thomas, Abnormal Schwann cell/axon interactions in the Trembler-J mouse. *J Anat* **190 (Pt 3)**, 423-432 (1997).
50. A. M. Robertson *et al.*, Comparison of a new pmp22 transgenic mouse line with other mouse models and human patients with CMT1A. *J Anat* **200**, 377-390 (2002).
51. E. W. Henry, J. S. Cowen, R. L. Sidman, Comparison of Trembler and Trembler-J mouse phenotypes: varying severity of peripheral hypomyelination. *J Neuropathol Exp Neurol* **42**, 688-706 (1983).
52. M. Budak *et al.*, Contrasting mechanisms for hidden hearing loss: Synaptopathy vs myelin defects. *PLoS Comput Biol* **17**, e1008499 (2021).
53. M. Kobel, C. G. Le Prell, J. Liu, J. W. Hawks, J. Bao, Noise-induced cochlear synaptopathy: Past findings and future studies. *Hear Res* **349**, 148-154 (2017).
54. M. Anniko, Early development and maturation of the spiral ganglion. *Acta Otolaryngol* **95**, 263-276 (1983).
55. J. Wang *et al.*, Myelination of the postnatal mouse cochlear nerve at the peripheral-central nervous system transitional zone. *Front Pediatr* **1**, 43 (2013).
56. Y. Sergeyenko, K. Lall, M. C. Liberman, S. G. Kujawa, Age-related cochlear synaptopathy: an early-onset contributor to auditory functional decline. *J Neurosci* **33**, 13686-13694 (2013).
57. A. E. Hickox, M. C. Liberman, Is noise-induced cochlear neuropathy key to the generation of hyperacusis or tinnitus? *J Neurophysiol* **111**, 552-564 (2014).
58. M. M. Asokan, R. S. Williamson, K. E. Hancock, D. B. Polley, Sensory overamplification in layer 5 auditory corticofugal projection neurons following cochlear nerve synaptic damage. *Nat Commun* **9**, 2468 (2018).
59. J. Resnik, D. B. Polley, Cochlear neural degeneration disrupts hearing in background noise by increasing auditory cortex internal noise. *Neuron* **109**, 984-996 e984 (2021).
60. M. Knipper, P. Van Dijk, I. Nunes, L. Ruttiger, U. Zimmermann, Advances in the neurobiology of hearing disorders: recent developments regarding the basis of tinnitus and hyperacusis. *Prog Neurobiol* **111**, 17-33 (2013).
61. W. A. Hossain, S. D. Antic, Y. Yang, M. N. Rasband, D. K. Morest, Where is the spike generator of the cochlear nerve? Voltage-gated sodium channels in the mouse cochlea. *J Neurosci* **25**, 6857-6868 (2005).
62. K. X. Kim, M. A. Rutherford, Maturation of NaV and KV Channel Topographies in the Auditory Nerve Spike Initiator before and after Developmental Onset of Hearing Function. *J Neurosci* **36**, 2111-2118 (2016).

63. M. A. Rutherford, N. M. Chapochnikov, T. Moser, Spike Encoding of Neurotransmitter Release Timing by Spiral Ganglion Neurons of the Cochlea. *The Journal of Neuroscience* **32**, 4773-4789 (2012).
64. E. J. Arroyo, S. S. Scherer, On the molecular architecture of myelinated fibers. *Histochem Cell Biol* **113**, 1-18 (2000).
65. J. M. Boggs, Myelin basic protein: a multifunctional protein. *Cell Mol Life Sci* **63**, 1945-1961 (2006).
66. R. Schaette, D. McAlpine, Tinnitus with a normal audiogram: physiological evidence for hidden hearing loss and computational model. *J Neurosci* **31**, 13452-13457 (2011).
67. A. A. Gabreels-Festen *et al.*, Charcot-Marie-Tooth disease type 1A: morphological phenotype of the 17p duplication versus PMP22 point mutations. *Acta Neuropathol* **90**, 645-649 (1995).
68. N. Giuliani, L. Holte, M. Shy, T. Grider, The audiologic profile of patients with Charcot-Marie Tooth neuropathy can be characterised by both cochlear and neural deficits. *Int J Audiol* **58**, 902-912 (2019).
69. C. L. Anzalone, S. Nuhanovic, A. P. Olund, M. L. Carlson, Cochlear Implantation in Charcot-Marie-Tooth Disease: Case Report and Review of the Literature. *Case Rep Med* **2018**, 1760978 (2018).
70. M. Kobayashi *et al.*, Cochlear implantation in patient with Charcot-Marie-Tooth disease. *Auris Nasus Larynx* **48**, 327-330 (2021).
71. Y. Uchida *et al.*, Age-related hearing loss and cognitive decline - The potential mechanisms linking the two. *Auris Nasus Larynx* **46**, 1-9 (2019).
72. T. D. Griffiths *et al.*, How Can Hearing Loss Cause Dementia? *Neuron* **108**, 401-412 (2020).
73. A. Chern, J. S. Golub, Age-related Hearing Loss and Dementia. *Alzheimer Dis Assoc Disord* **33**, 285-290 (2019).
74. R. Fledrich *et al.*, NRG1 type I dependent autoparacrine stimulation of Schwann cells in onion bulbs of peripheral neuropathies. *Nat Commun* **10**, 1467 (2019).
75. Z. Sahenk, B. Ozes, Gene therapy to promote regeneration in Charcot-Marie-Tooth disease. *Brain research* **1727**, 146533 (2020).
76. S. Belin *et al.*, Neuregulin 1 type III improves peripheral nerve myelination in a mouse model of congenital hypomyelinating neuropathy. *Hum Mol Genet* **28**, 1260-1273 (2019).
77. C. Pisciotta, D. Pareyson, Gene therapy and other novel treatment approaches for Charcot-Marie-Tooth disease. *Neuromuscul Disord* **33**, 627-635 (2023).
78. B. Ozes *et al.*, AAV1.NT-3 gene therapy for X-linked Charcot-Marie-Tooth neuropathy type 1. *Gene Ther* **29**, 127-137 (2022).
79. G. Wan, M. E. Gomez-Casati, A. R. Gigliello, M. C. Liberman, G. Corfas, Neurotrophin-3 regulates ribbon synapse density in the cochlea and induces synapse regeneration after acoustic trauma. *Elife* **3** (2014).

Figures

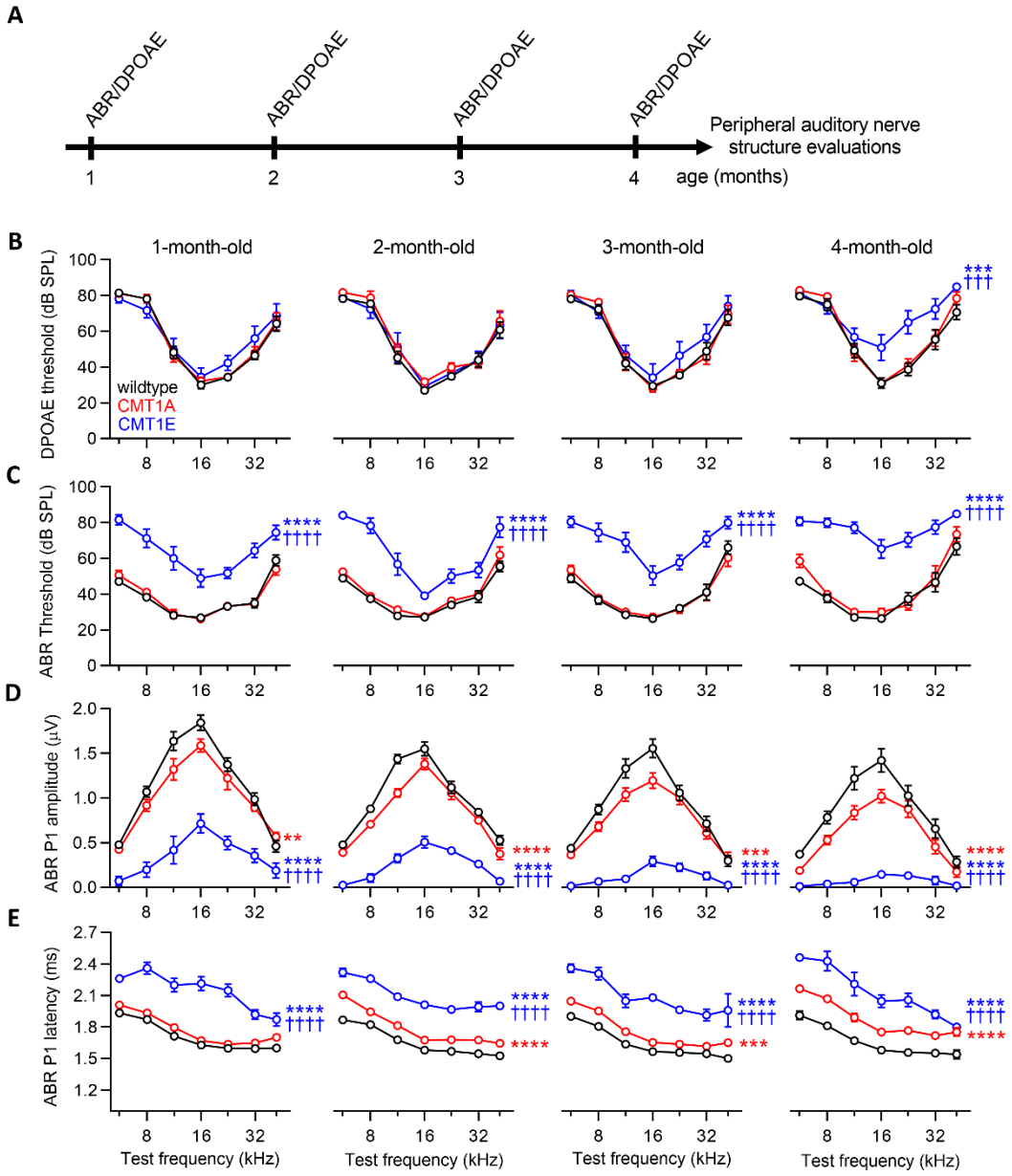

Figure 1. CMT1A mice have progressive hidden hearing loss whereas CMT1E have early onset overt hearing loss. (A) Timeline of the experimental design. CMT1A, CMT1E and wildtype C57BL/6J littermates were used. ABRs and DPOAEs were recorded at 1, 2, 3 and 4 months of age. After the last ABR and DPOAE tests, cochleae were collected and processed for either transmitted electron microscopy or immunohistochemistry followed by confocal microscopy to evaluate structural changes at the level of the peripheral auditory nerve. (B) CMT1A mice have normal DPOAE thresholds at all time points while CMT1E mice show mild DPOAE threshold shifts starting at 4 months of age. (C) CMT1A mice have normal ABR thresholds while in CMT1E animals they are increased at all time points when compared with wildtype littermates. (D) ABR peak I amplitudes are progressively reduced in both CMT1 groups

compared with wildtype mice; however, these reductions are more severe in CMT1E mice compared with CMT1A mice (also see Figure S1). (E) ABR peak I latencies are longer in both CMT1 groups compared with wildtype mice, yet CMT1E animals show a more severe phenotype compared with CMT1A mice. Wildtype n = 14–19 mice; CMT1A n = 8–11 mice; CMT1E n = 6–12 mice. Two-way ANOVA followed by Tukey's multiple comparisons test was used to evaluate statistical differences among the experimental groups at each individual time point for either DPOAE threshold, ABR threshold, ABR peak I amplitude or ABR peak I latency. ** $p < 0.01$; *** $p < 0.001$; **** $p < 0.0001$ vs wildtype mice; ††† $p < 0.001$; †††† $p < 0.0001$ vs CMT1A mice. Error bars represent SEM.

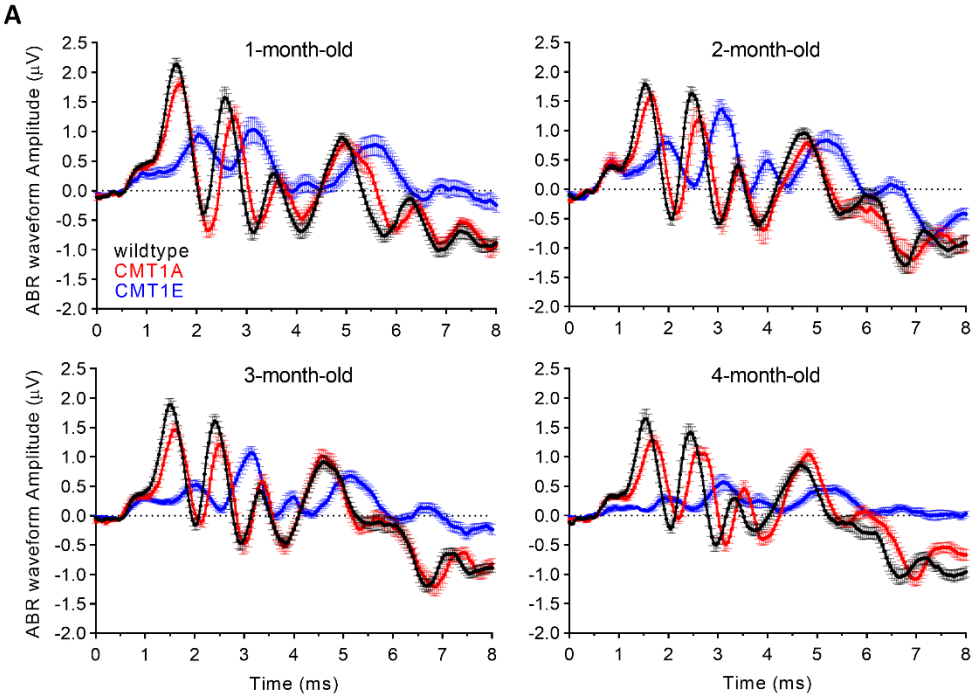

Figure 2. Distinct effects of CMT1A and CMT1E on signaling along the ascending auditory pathway. (A) Mean ABR waveforms recorded at 1, 2, 3 and 4 months of age show a progressive delay and reduction of the first ABR peak in both CMT1 mouse models. CMT1E phenotype is more severe than in CMT1A mice, affecting the later ABR peaks along the ascending auditory pathway. ABRs shown here are group means in response to 16 kHz tone pips at 80 dB SPL. Wildtype n = 14–19 mice; CMT1A n = 8–11 mice; CMT1E n = 6–12 mice. Error bars represent SEM.

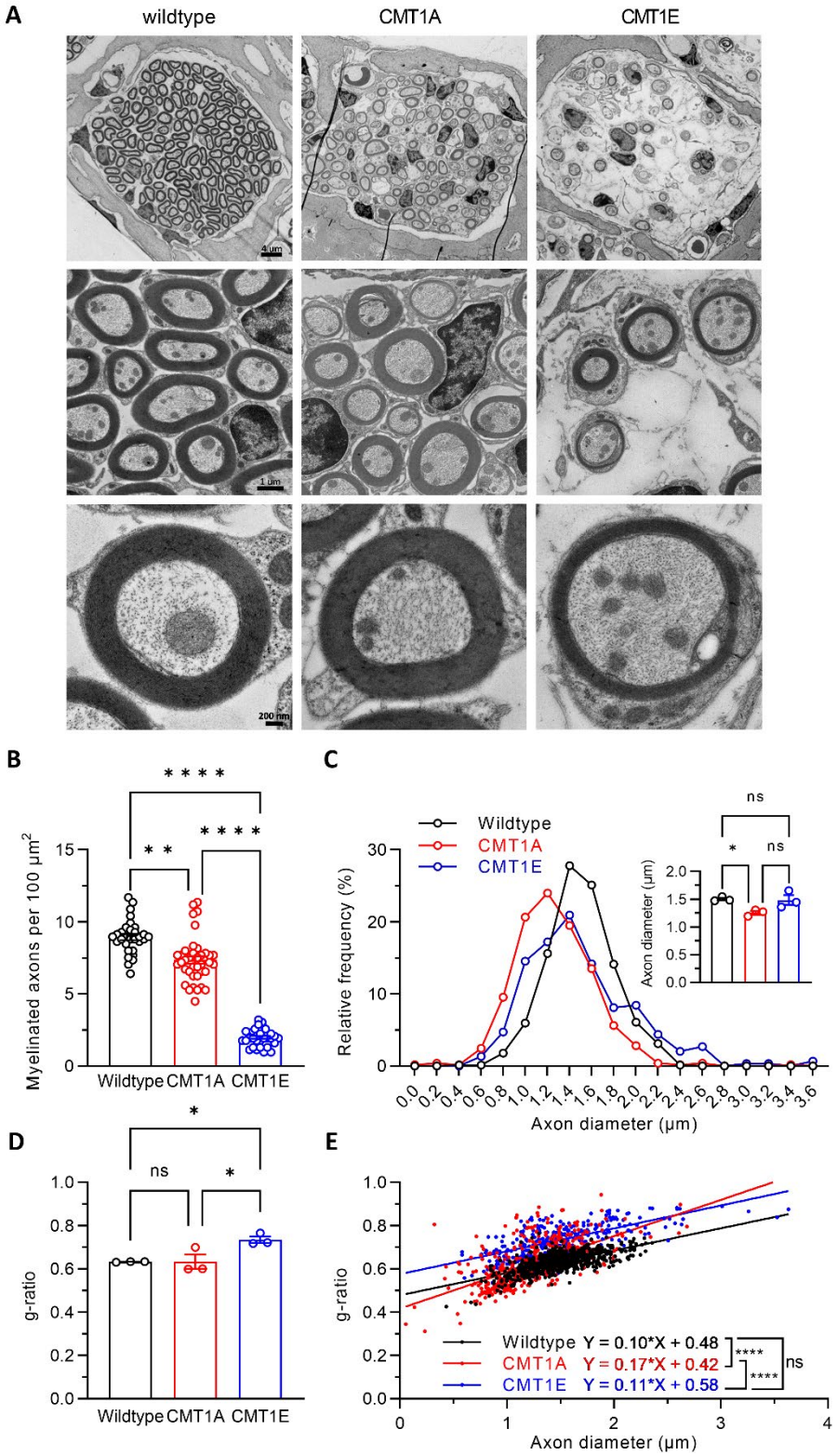

Figure 3. CMT1A and CMT1E mice have distinct myelin and axonal pathologies. (A) Representative electron micrographs of sections through the osseous spiral lamina showing an axon bundle (top), a high magnification image of the axons (middle) and an individual

myelinated axon image (bottom) from 4-month-old wildtype (left), CMT1A (center) and CMT1E (right) mice. (B) CMT1A and CMT1E animals have different degrees of myelinated axons loss, 18 % and 78 % respectively compared to wildtype mice. (C) Frequency histogram showing that CMT1A mice have an increased number of small diameter axons than wildtype mice. Inset: CMT1A mice have a 16% reduction in axon diameter vs wildtype. (D) CMT1E mice have decreased myelin thickness (g-ratio = 0.735) compared with wildtype (g-ratio = 0.633) and CMT1A mice (g-ratio = 0.633). (E) CMT1E hypomyelination is independent of axon diameter while CMT1A mice have an increased steepening in the regression line in the g-ratio vs axon diameter graph. n = 3 cochleae per genotype. One cochlea from each mouse was analyzed and quantifications were done at the 16 kHz region. Quantification of myelinated axon densities was analyzed by Kruskal-Wallis test followed by Dunn's multiple comparisons test. Quantification of axon diameters and g-ratios were analyzed by one-way ANOVA followed by Tukey's multiple comparisons test. Linear regression and differences among slopes of axon diameters vs g-ratio plots were obtained with GraphPad Prism simple linear regression test. * $p < 0.05$; ** $p < 0.01$; **** $p < 0.0001$. Error bars represent SEM.

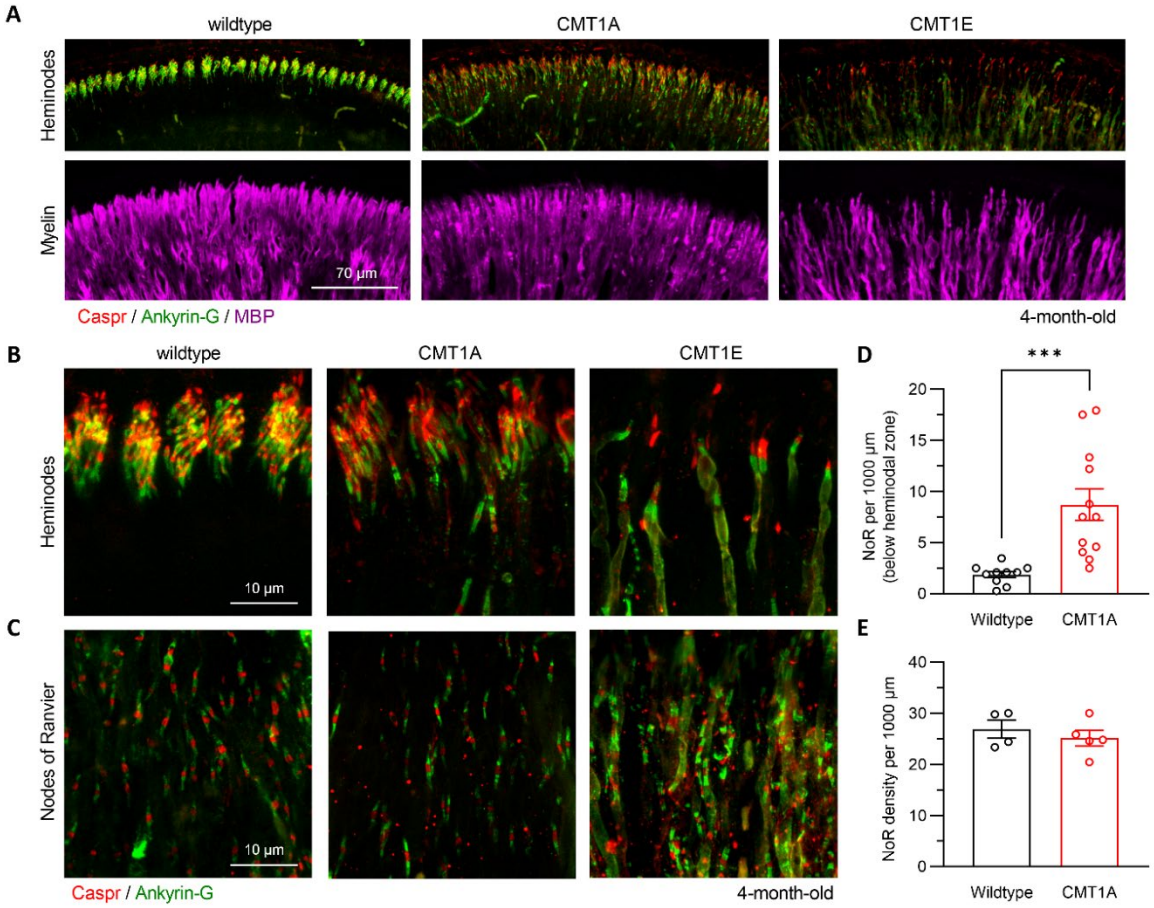

Figure 4. CMT1A and CMT1E mice have nodes of Ranvier and heminodes abnormalities. (A) Representative low magnification images showing that the AN heminodes adjacent to the organ of Corti (top) and the AN myelin in the osseous spiral lamina (bottom) are disrupted in CMT1A (center) and CMT1E (right) cochleae at 4 months old compared with wildtype mice (left). (B) High magnification images showing the heminodes and nodes of Ranvier and (C) the nodes of Ranvier at the 16 kHz cochlear region from wildtype (left), CMT1A (center) and CMT1E (right) mice. (D) CMT1A mice have increased number of nodes of Ranvier-like structures in the 20 µm area below the disrupted heminodes compared with wildtypes. (E) The density of nodes of Ranvier at the level of the osseous spiral lamina in CMT1A mice is not affected. Samples were immunolabelled for paranodes (Caspr); nodes of Ranvier (Ankyrin-G) and myelin (MBP). Wildtype n = 4-10 cochleae; CMT1A n = 5-12 cochleae; CMT1E n = 4-6 cochleae. One cochlea from each mouse was analyzed and quantifications were done at the 16 kHz region. Quantification of nodes of Ranvier density in either the 20µm below the heminodal area or in the osseous spiral lamina region were analyzed by two-tailed t-test. Quantification of heminodes and nodes of Ranvier in CMT1E mice was not possible due to the severe axonal damage exhibited. *** $p < 0.001$. Error bars represent SEM.

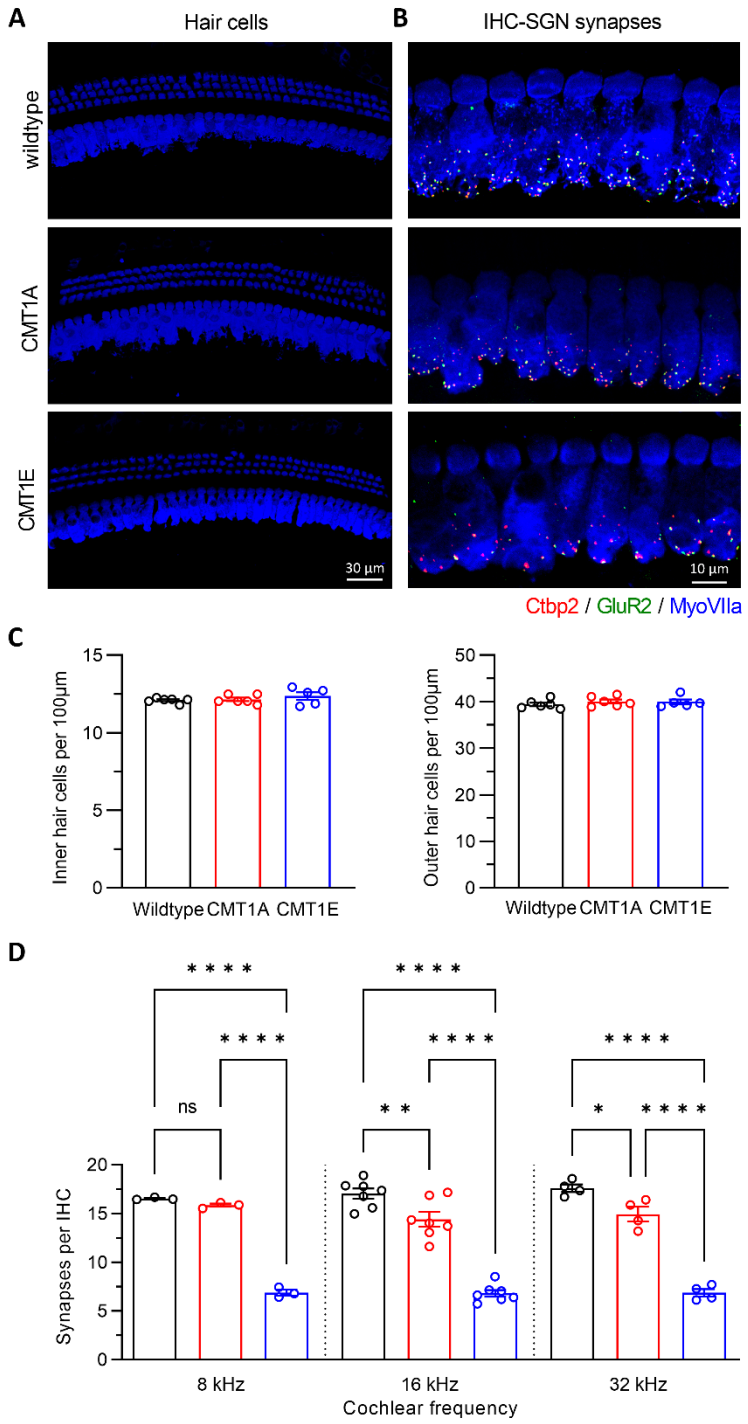

Figure 5. CMT1A and CMT1E mice have different degrees of IHC-SGN synapse loss without hair cell loss. Representative confocal images of hair cells (A) and IHC-SGN synapses (B) at the 16 kHz region of wildtype (top), CMT1A (middle) and CMT1E (bottom) cochleae immunolabeled for hair cells (MyoVIIa), pre-synaptic ribbons (Ctbp2) and post-synaptic receptor patches (GluR2). (C) Inner (left) and outer (right) hair cells survival is not affected by these two different CMT1 mutations. (D) CMT1A mice have mild IHC-SGN synapse loss at 16 and 32 kHz areas, compared with wildtype mice. CMT1E IHC-SGN synapse density

is more severely reduced than in CMT1A. Wildtype n = 3-7 cochleae; CMT1A n = 3-7 cochleae; CMT1E n = 3-7 cochleae. One cochlea from each mouse was analyzed. IHC-SGNs synapse density was analyzed by one-way ANOVA followed by Sidak's multiple comparisons test. Quantification of inner and outer hair cells was analyzed by Kruskal-Wallis test followed by Dunn's multiple comparisons test. * $p < 0.05$; ** $p < 0.01$; **** $p < 0.0001$. Error bars represent SEM.

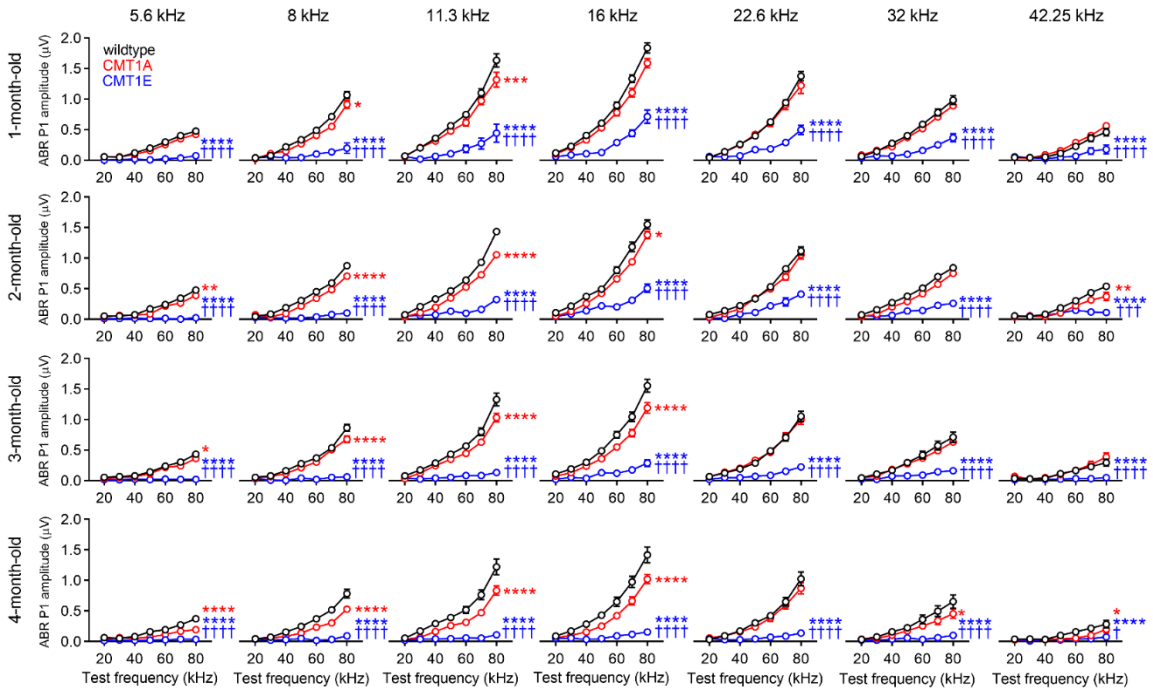

Figure S1. ABR input-output functions reveal difference between CMT1A and CMT1E auditory phenotypes. ABR peak I amplitudes in CMT1A animals show progressive defects, staring at 8-11 kHz and expanding to other frequencies with aging. In contrast, all frequency areas are severely affected in CMT1E mice already at one month old. Wildtype n = 14–19 mice; CMT1A n = 8–11 mice; CMT1E n = 6–12 mice. Two-way ANOVA followed by Tukey's multiple comparisons test was used to evaluate ABR peak I amplitude statistical differences among the groups at every individual time point and tested frequency. * $p < 0.05$; ** $p < 0.01$; *** $p < 0.001$; **** $p < 0.0001$ vs wildtype mice; † $p < 0.05$; ††† $p < 0.001$; †††† $p < 0.0001$ vs CMT1A mice. Error bars represent SEM.

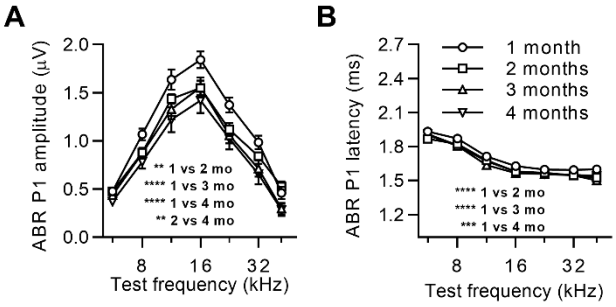

Figure S2. C57BL/6J wildtype mice have early onset ABR peak I amplitude decline. (A) Wildtype mice show a small but significant progressive decline in ABR peak I amplitudes. (B) ABR peak I latencies shorten between 1 and 2 months old, possibly due to the maturation of AN myelination. Wildtype n = 14–19 mice. Two-way ANOVA followed by Tukey's multiple comparisons test was used to evaluate statistical differences among the experimental groups for either ABR peak I amplitude or ABR peak I latency. ** $p < 0.01$; **** $p < 0.0001$. Error bars represent SEM.